A UFO Seen Edge-on? Resolving Ultrafast Outflow Emission on ∼200 pc Scales with Chandra in the Active Nucleus of Mrk 34

W. Peter Maksym[1] , Martin Elvis[1] , Giuseppina Fabbiano[1] , Anna Trindade Falcão[1] , Steven B. Kraemer[2] ,
Travis C. Fischer[3] , D. Michael Crenshaw[4] , and Thaisa Storchi-Bergmann[5]
[1] Center for Astrophysics | Harvard & Smithsonian, 60 Garden St., Cambridge, MA 02138, USA; walter.maksym@cfa.harvard.edu
[2] Institute for Astrophysics and Computational Sciences, Department of Physics, The Catholic University of America, Washington, DC 20064, USA
[3] Space Telescope Science Institute, 3700 San Martin Drive, Baltimore, MD 21218, USA
[4] Department of Physics and Astronomy, Georgia State University, Astronomy Offices, 25 Park Place, Suite 600, Atlanta, GA 30303, USA
[5] Departamento de Astronomia, Universidade Federal do Rio Grande do Sul, IF, CP 15051, 91501-970 Porto Alegre, RS, Brazil
Received 2022 September 28; revised 2023 April 26; accepted 2023 May 9; published 2023 July 12

Abstract

We present Chandra ACIS imaging spectroscopy of the nucleus of the Seyfert 2 Galaxy Mrk 34. We identify spatially and spectrally resolved features in the band that includes Fe Kα, Fe XXV, and Fe XXVI. These features suggest high-velocity ($\gtrsim$15,000 km s^{-1} line-of-sight) material spanning $\sim$0.″5, within $\sim$200 pc of the nucleus. This outflow could have deprojected velocities $\sim$12–28$\times$ greater than the [O III]-emitting outflows, and could potentially dominate the kinetic power in the outflow. This emission may point to the origins of the optical and X-ray winds observed at larger radii, and could indicate a link between ultrafast outflows and AGN feedback on $\gtrsim$kiloparsec scales.

Unified Astronomy Thesaurus concepts: AGN host galaxies (2017); X-ray active galactic nuclei (2035); Seyfert galaxies (1447)

1. Introduction

Active galactic nuclei (AGNs) are observed to generate jets and winds, which are thought to play critical roles in galaxy evolution in the form of "feedback," which may stimulate or suppress star formation via the expulsion of star-forming gas from the host galaxy by regulating the temperature and density of the remaining interstellar medium (ISM) and by affecting the rate at which the nuclear black hole accretes matter.

AGN feedback is likely a complex, multistage process (Hopkins & Elvis 2010; Gaspari & Sądowski 2017; Harrison et al. 2018). Ultrafast outflows (UFOs) seen in absorption (Laha et al. 2021) reach $\gtrsim$0.2c, which is clearly capable of expelling ISM. But even the closest UFOs are spatially unresolved, and inferences that such velocities are sustained beyond ∼parsec scales therefore require indirect constraints. Large-scale outflows in the host ISM may reach $\gtrsim$kiloparsec scales but rarely exceed ∼2000 km s^{-1} in spatially resolved optically emitting or molecular gas (e.g., Fischer et al. 2013). In the case of [O III] kinematics, only velocities in excess of typical rotational velocities (∼100–300 km s^{-1}) can be attributed to outflows capable of producing effective AGN feedback (Fischer et al. 2017). Understanding the transition between these two regimes is critical to modeling the physics of AGN feedback, but this interface regime is particularly challenging to observe due to the the low emissivity of hot plasmas and the instrumental limits of modern X-ray telescopes.

A growing number of observations indicate evidence for such an interface region at ∼100 pc scales. BALQSO spectra indicating UFO-like velocities may be common at $\gtrsim$100 pc scales (Arav et al. 2018). Possible evidence for multiphase gas

entrained in UFOs has also been seen in unresolved spectra at $\gtrsim$100 pc scales (Serafinelli et al. 2019).

With the availability of increasingly deep Chandra observations, the Fe Kα complex has recently become a promising tool for studying spatially resolved AGN–host interactions on subkiloparsec scales. This complex includes neutral Fe Kα (6.4 keV rest energy) as well as the helium-like Fe XXV triplet at ∼6.7 keV and the 7.0 keV Lyα of hydrogenic Fe XXVI. A growing number of observations of local Seyfert 2 galaxies, like NGC 6240, ESO 428-G014, IC 5063, NGC 3393 and others, have shown extended hard (3–8 keV) emission, extending to ∼kiloparsec scales in some cases (Wang et al. 2014; Fabbiano et al. 2017, 2018a, 2018b, 2019; Maksym et al. 2017, 2019; Jones et al. 2020; Ma et al. 2020; Jones et al. 2021; Travascio et al. 2021), as well as reflected Fe Kα (Fabbiano et al. 2017, 2019; Jones et al. 2020; Travascio et al. 2021) and Fe XXV excited via collisions between AGN outflows and molecular clouds in the ISM (Travascio et al. 2021).

Mrk 34 ($z = 0.05080$, Hubble distance $D_H = 209$ Mpc, $1'' = 1014$ pc for $H_0 = 71$ km s^{-1}; Revalski et al. 2018) is known to have powerful outflows associated with spatially extended radio emission and narrow-line emission in the optical and X-rays (Falcke et al. 1998; Revalski et al. 2018, 2019; Trindade Falcão et al. 2021; Bessiere & Ramos Almeida 2022). A radial increase in outflow gas mass in Mrk 34, with increasing r toward $r \sim 500$ pc, led Revalski et al. (2018, 2019) to suggest that [O III] gas is accelerated in situ. But models by Trindade Falcão et al. (2021) indicate that the [O III] gas may originate from a lower-ionization, higher-density state, and that this process may be facilitated by an X-ray wind which could be more kinematically powerful than the optical gas by a factor of ∼50.

Mrk 34 is highly obscured (log [n_H/cm^{-2}] $\gtrsim$ 24.3; Gandhi et al. 2014; Zhao et al. 2020), and is therefore another excellent candidate for similar spatial mapping of extended hard emission. In this paper, we examine spatially resolved emission

in Chandra observations of Mrk 34 in the 5.5–7.0 keV band. We find evidence for high-velocity Fe outflows, which may provide a link between UFOs seen in absorption and kiloparsec-scale winds seen in emission.

2. Observations and Processing

Mrk 34 was observed by Chandra with ACIS on 2017 January 30 to spatially resolve X-ray emission from termination shocks in two of the most powerful kinematic outflows with angular scales accessible to Chandra (Obsid 18121; PI: Elvis). Detailed spatial and spectroscopic analysis of the other program target, Mrk 78, was published by Fornasini et al. (2022) and is similarly in preparation for the Mrk 34 observations (W. P. Maksym et al. 2023, in preparation). Data were reduced using standard Chandra methods and v4.13 of the `CIAO` package (Fruscione et al. 2006), with CALDB v4.9.3. We reprocessed the data using `chandra_repro` and found no significant background flares. The useful exposure time totaled 99.1 ks. We used `wavdetect` to identify matches between field X-ray sources and the Sloan Digital Sky Survey (Ahn et al. 2012), and cross-registered the astrometry with `wcs_match` and `wcs_update`. We excluded matches with residuals $>2''$, leaving three sources with positional uncertainties of $\sim 0''.1$ each.

Mrk 34 was previously observed by the Very Large Array (VLA) on 1991 September 1 in the X band (8.44 GHz) as part of program AW0278. We used the processed NRAO archival image, which has a beam size of $0''.2713$ and rms sensitivity of 26 μJy.

3. Data Reduction and Results

3.1. Nuclear Spectroscopy

In order to identify useful line-emission features for sub-arcsecond imaging, we initially assumed the AGN to be located at the centroid of the 6–7 keV band for the purpose of spectroscopy. We extracted a spectrum of the nucleus for a $r = 2''$ circle at this position (J2000 [α, δ] = [$10^h34^m08^s.59$, $+60°01'52''.1$]), which is comparable to the $\sim$90% encircled energy radius for this band. The spectrum has five photons per energy bin, which when fitted with `lstat` (Loredo 1992) is a useful compromise between the energy resolution of unbinned `cstat` fitting (Cash 1979) and the ability to subtract an unmodeled background with χ^2 fitting.

We fit this spectrum with `XSpec`, excluding the soft emission below 3 keV (observer), which is typically dominated by ionized reflection or emission from collisionally excited plasma on scales reaching the extended narrow-line region (ENLR $\gtrsim$ parsec scales; see, e.g., Maksym et al. 2017, 2019; and, for Mrk 34, Trindade Falcão et al. 2021 and W. P. Maksym et al. 2023, in preparation).

We can model the continuum with a simple absorbed power-law model fit to 3–8 keV (observer), which excludes the Fe Kα complex by ignoring data points between 5.5 and 7.0 keV (observer). We then model an expected neutral Fe Kα contribution to the observed excess emission by adding a Gaussian at $E = 6.39$ keV (rest).

The best fit for this model produces an effective 5.5–7.0 keV (observer) $\Delta\chi^2/\text{DoF} = 28.14/28$ and Gaussian width $\sigma = (13 \pm 2) \times 10^3\,\text{km s}^{-1}$. This is an order of magnitude larger than velocities characteristic of the torus and the narrow-line region and is sufficiently broad that it would be affected if
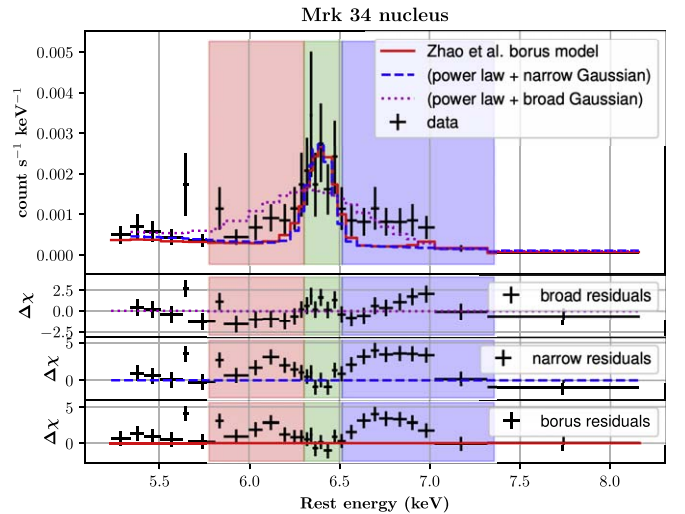
Figure 1. Chandra 5–8 keV spectrum for $r < 2''$ of the Mrk 34 nucleus. The red solid model uses the borus and absorbed power-law components used by Zhao et al. (2020, red line), normalized to the Fe Kα peak between 6.3 keV and 6.5 keV (rest frame, green shading) and with no thermal plasma component. Magenta dots and blue dashes indicate a simpler absorbed power law plus Gaussian, with the Gaussian width free to vary (magenta dots) or assumed narrow and unresolved (blue dashes). All models produce systematic residuals. Residuals compared to Zhao et al. (2020) and the narrow Gaussian are significant compared to the red (5.8–6.3 keV rest) and blue (6.5–7.4 keV rest) of Fe Kα, and include the rest energies of Fe XXV and Fe XXVI.

Fe XXV contributes significantly. The residual structure also suggests that a narrow Fe Kα line should be considered.

When we assume a single unresolved Gaussian ($\sigma = 0.01$ keV) at Fe Kα, residual excess "wings" are seen immediately redward (5.8–6.3 keV rest) and blueward (6.5–7.0 keV rest) of Fe Kα, suggestive of outflows at $v \sim \pm 15,000\,\text{km s}^{-1}$ (assuming an ionization state of Fe XVII at most; see Figure 1).

Using additional Gaussian components, we estimate the (red, blue) wing to have [3.0σ, 4.1σ] significance and equivalent width EW = [0.43 ± 0.14 keV, 0.99 ± 0.24 keV]. The red-wing model excess is fit as a Gaussian at $\sim$6.08 keV and therefore also inconsistent with a Compton shoulder feature at $\sim$6.25 keV (rest). The center of the blue wing is at $\sim$6.76 $\pm$ 0.05 keV (rest), and is therefore consistent with Fe XXV at $v \lesssim 2000\,\text{km s}^{-1}$. Narrow Fe XXVI is consistent with a $\sim$1σ detection, and EW = 0.16 $\pm$ 0.16 keV.

For comparison, in Figure 1 we show also a fit to a physically motivated model that also incorporates very hard X-ray constraints (>8 keV).

We also adopt a variant of the Zhao et al. (2020) model, which used a combination of an AGN torus model (`borus02`; Baloković et al. 2018) and absorbed power laws with high-energy cutoffs in a joint fit to this data set and NuSTAR.

Zhao et al. (2020) fit this model using several types of constraints, but we begin with the "free" fit parameters from Zhao et al.'s (2020) Table 2. These parameters are comparable to the other configurations that they consider, which assume [O III]-derived constraints or 60° torus inclination. In order to avoid model-dependent contamination of the hard continuum model via constraints from complex soft (0.3–3 keV) extended emission, we excluded the Zhao et al. (2020) soft thermal plasma component and froze all other parameters except a normalization constant. The spectral shape of the unresolved obscured emission is therefore constrained by the NuSTAR

data. However, with $N_H \gtrsim 10^{25}\,\mathrm{cm}^{-2}$ from the torus the hard Chandra continuum effectively reduces to the absorbed power law.

Excluding the Fe Kα complex (∼5.5−7.0 keV observer) from the fit tends to produce excess in the 6.0–6.2 keV band for the Zhao et al. (2020) model, corresponding to narrow emission from neutral Fe Kα at 6.4 keV (rest). Leaving the `borus02` Fe abundance free can reduce this excess, but with unphysically low values for an AGN nucleus (∼0.4). This suggests that the binning scheme used by Zhao et al. (2020) is too coarse (20 counts bin^{-1}) to spectrally resolve the relevant substructure seen here in the Fe Kα complex and continuum.

Figure 1 shows that the excess "wing" emission observed above the power law is nearly identical compared to this more physically motivated model, and therefore does not appear to be strongly model dependent.

3.2. Multiband Imaging

In order to examine whether the possible Fe Kα wings have spatial extent and structure, we produced images dividing Fe Kα into three bands ("red wing," 5.8–6.3 keV rest; "core," 6.3–6.5 keV; "blue wing," 6.5–7.4 keV). For comparison, we have also included a hard "continuum" band (3.2−5.8 keV rest), which has long been broadly assumed to be point-like in AGNs but has recently been observed to have extent in numerous instances (e.g., Maksym et al. 2017; Ma et al. 2020; Jones et al. 2021).

We binned the photon events at one-sixteenth native ACIS pixel scale (0″.0625) and applied Gaussian smoothing with $r = 7$ pixels (0″.215). We also used `dmimgadapt` to generate adaptively smoothed images that preserve features with $\geqslant 9$ photon counts (∼3σ significance). VLA radio contours are overlaid to enable comparison to analysis of the Mrk 34 outflows in other work. We also used a spectrum of the nucleus, `marx` (Davis et al. 2012), and SAOTrace[6] to simulate an event file of the ACIS point-spread function (PSF) with ∼2600 5.5–7.0 keV counts at $r < 2''$ (∼10× observed).

Figure 2 shows the single-band results of this smoothing (column #1 for Gaussian smoothing, column #2 for adaptive smoothing). Figure 2, column #3 shows radial profiles of the Mrk 34 nucleus for $r \leqslant 1''.0$, binned at $\Delta r = 0''.1$ intervals. The band-specific centroid for each unsmoothed photon image is set to $r = 0$ and compared against the band-specific PSF simulation. The PSF is shown with counts and errors according to three different normalizations: the median surface brightness for the $0''.0 < r \leqslant 0''.5$ bins, the $r \leqslant 0''.1$ bin only, and the total counts.

The hard continuum (3.2–5.8 keV, 114 counts for $r < 2''.0$) shows two features roughly NW and SE of the band centroid, separated by ∼1 PSF FWHM. The radial profile of this band shows a central $r \leqslant 0''.1$ bin with a significant deficit when normalized to match the PSF wings, and its χ^2 test is inconsistent with the PSF at 3.0σ.

The red wing (5.8–6.3 keV, 41 counts for $r < 2''.0$) also shows significant resolved structure. It also has a significant radial profile deficit at $r \leqslant 0''.1$. The χ^2 radial profile alone rejects the PSF model at only 90% significance, but there is also significant azimuthal structure with a N–S orientation. When the $0''.1 < r < 1''.0$ data are divided into four equal N, S, E, and W bins, the PSF model is rejected at 3.1σ.

PSF comparisons fail to show extent within the blue wing (6.5–7.4 keV rest, 42 counts, χ^2 null-hypothesis probability $p \sim 0.5$) and core Fe Kα band (6.3–6.5 keV, 46 counts, $p \sim 0.2$).

For cross-band comparison, we produced an image (Figure 3) which overlays the Fe Kα bands (red, 5.8–6.3 keV rest; green "core," 6.3–6.5 keV; blue, 6.5–7.4 keV), as well as centroid positions for the Fe Kα bands and the hard continuum.

Positional uncertainties are determined via `dmstat` and are typically ∼0″.1. The centroid positions of the red, core, and blue wings of the Fe Kα complex all vary by $\gtrsim 2\sigma$ from each other. The hard continuum centroid is consistent with the other bands, but its large positional uncertainty is attributable to observed NW–SE substructure larger than the PSF uncertainty in the Fe Kα complex bands. There is therefore spatial structure not only within bands (in the hard continuum and red wing) but via intraband comparison across all four bands (including also the Fe Kα core) at the limits of the Chandra PSF.

In order to further quantify this observed energy-dependent spatial structure in terms of observed N–S trends (and for comparison against outflow structures observed in the radio and optical; e.g., Revalski et al. 2018), we calculated the median photon energy as a function of δ offset in the 5.8–7.4 keV rest band for a series of $1'' \times 0''.5$ boxes in (α, δ), each offset by 0″.1 in δ. The result is shown in Figure 4, along with a similar energy profile for the PSF simulation. The median energy of the Mrk 34 nucleus shifts almost monotonically by 288 eV (∼13,000 km s^{-1}) over 1″.2 (∼1.2 kpc). This exceeds both the ACIS-S energy FWHM of ∼160 eV at 5.9 keV, and the in-band simulated PSF FWHM of ∼0″.4. The bins' median energies for the PSF simulation span $\lesssim 100$ eV. This span is greatest between the core and larger radii, and likely dominated by the tendency of the PSF to spread at larger energies.[7]

4. Discussion

Chandra ACIS imaging spectroscopy of the Mrk 34 nucleus shows evidence for spatially resolved ($D \gtrsim 500$ pc) excess emission in the red and blue wings of Fe Kα, which corresponds to projected velocities of ∼15,000 km s^{-1}, and is robust against both physically motivated broadband models (Zhao et al. 2020) and a simple power-law continuum. Given the Compton-thick column density inferred by Zhao et al. (2020), this spectral structure is unlikely to be attributable to the accretion disk, which would be highly obscured. Rather, the Fe Kα complex emission should be emitted from the torus— which would not be extended, given $r \gtrsim$ few × 0.6 pc from the bolometric luminosity (Trindade Falcão et al. 2021) and the dust sublimation radius (Nenkova et al. 2008, 2008)—or from beyond the torus.

The hard continuum and Fe Kα complex show clear evidence for spatial extent, both within bands (in the hard continuum and red wing) and across bands (including also the Fe Kα core), ruling out a torus origin. We observe a spatially resolved trend of increasing median photon energy from S–N within the Fe Kα complex. This trend and the observed N–S structure within the red wing suggest a southern structure dominated by red-wing photons, as well as a northern structure which is more spectroscopically complex, containing the blue wing and possibly contributions from other parts of the Fe Kα complex. This structure may be related to the dual-peak structure seen in the hard continuum.
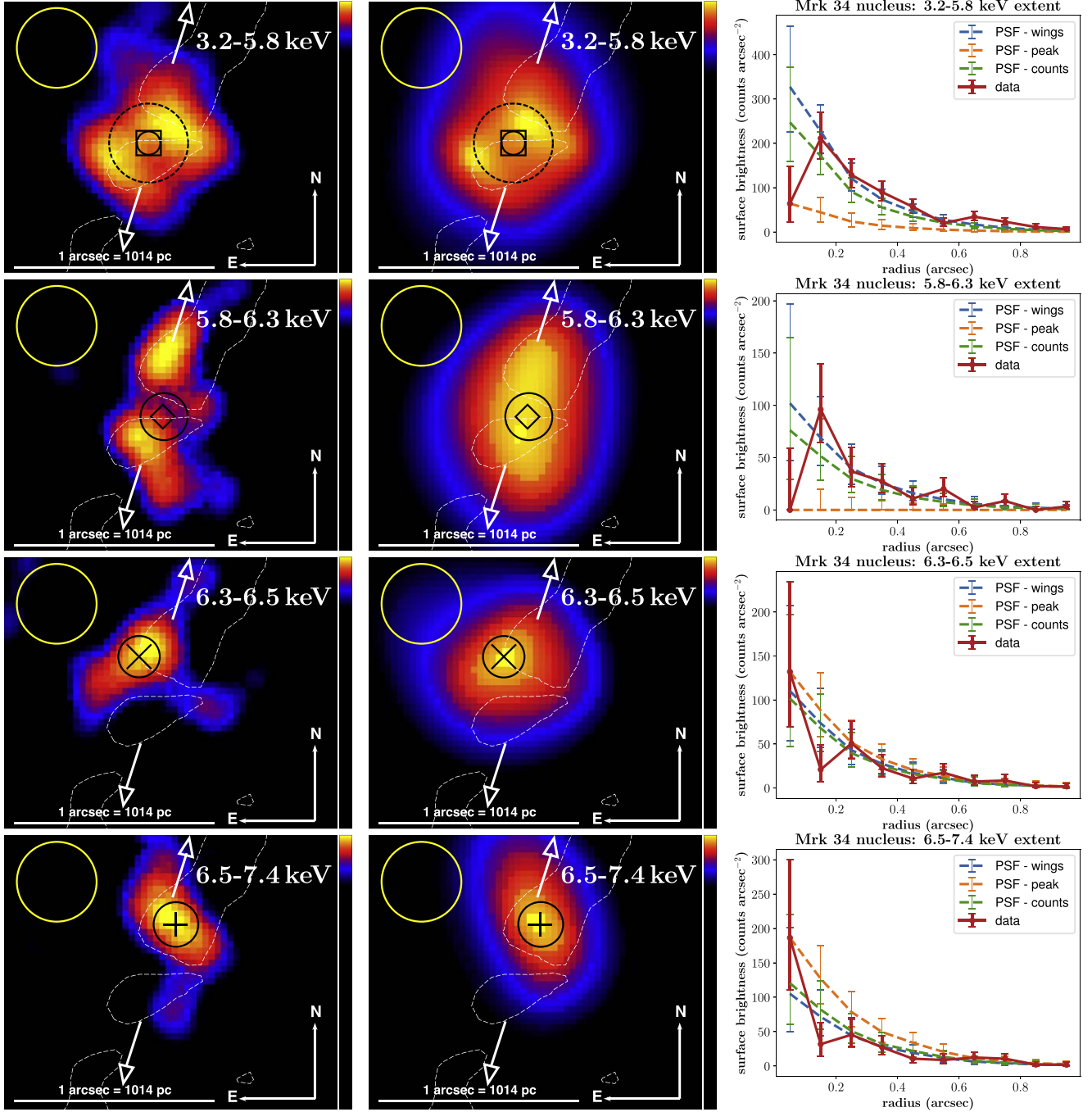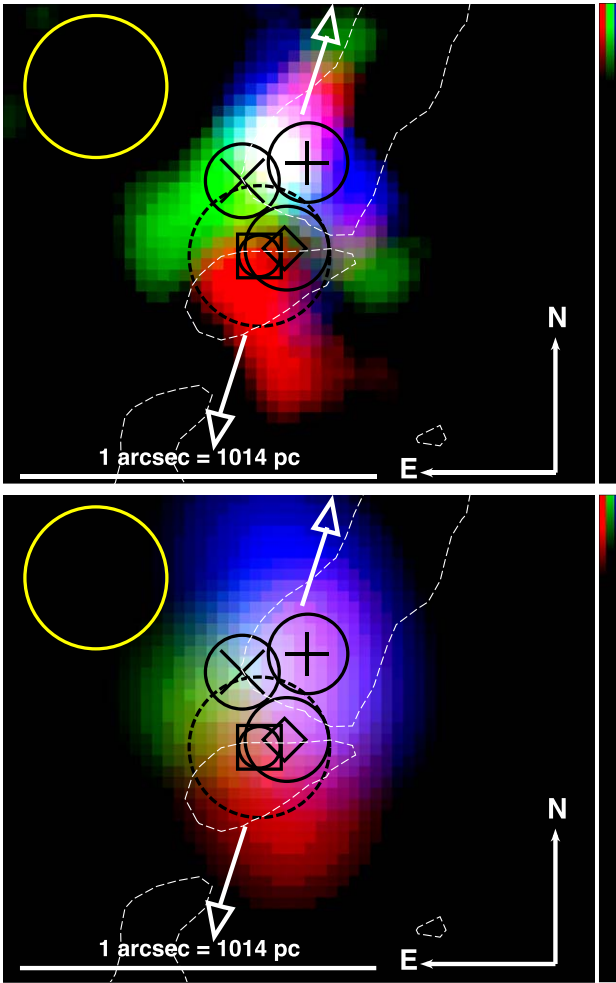

Figure 2. Top to bottom: smoothed images and source extent plots, with rest-wavelength bands as labeled. The 3.2–5.8 keV and 5.8–6.3 keV bands show statistically significant deficits in the core relative to the PSF models. The extended emission evident under different methods of image smoothing is therefore not an artifact of the PSF or photon scatter. Left column: images of the Mrk 34 nucleus binned at one-sixteenth native ACIS pixel scale, with $r = 0\rlap{.}''215$ Gaussian smoothing applied. White overlaid contours are from 8.44 GHz VLA imaging. Black circles show the centroid positional uncertainty as determined by `dmstat`. The diameter of the yellow solid circle indicates the FWHM of the Chandra PSF across these bands ($D_{\mathrm{FWHM}} \sim 0\rlap{.}''40$). White solid arrows indicate the direction and position angle of the fastest-moving optically emitting material according to Revalski et al. (2018). Center column: as before, but data are adaptively smoothed to preserve features with at least nine photon counts. Right column: radial profiles for band-specific data (solid red) compared to PSF models (dashed) with counts and errors normalized according to median surface brightness for $0\rlap{.}''0 < r \leqslant 0\rlap{.}''5$ bins (wings, blue), the $0\rlap{.}''0 < r \leqslant 0\rlap{.}''1$ bin only (peak, orange), and total counts (counts, green).

The representative scale of the multiband N–S structure between the centroid of the blue wing and the southernmost resolved features of either the hard continuum or the red wing is $D \gtrsim 0.4''$, which corresponds to $r \gtrsim 200$ pc. We can assume bilateral symmetry from a central nucleus and adopt the same bicone geometry as found for the [O III] outflow. The projected morphological orientation of the Fe Kα complex is consistent with

structure described in other bands (Falcke et al. 1998; Fischer et al. 2013; Revalski et al. 2018; Trindade Falcão et al. 2021).
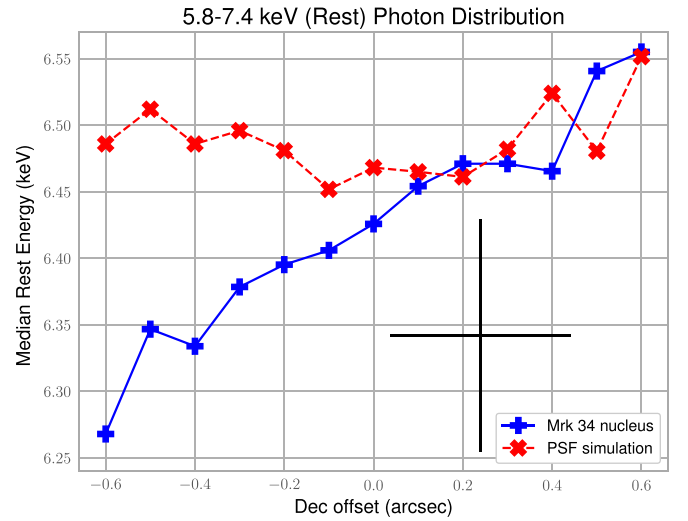
4.1. Low-ionization Fluorescence

Although some of the blue wing may arise from thermal outflows, fluorescence provides a simpler explanation than thermal
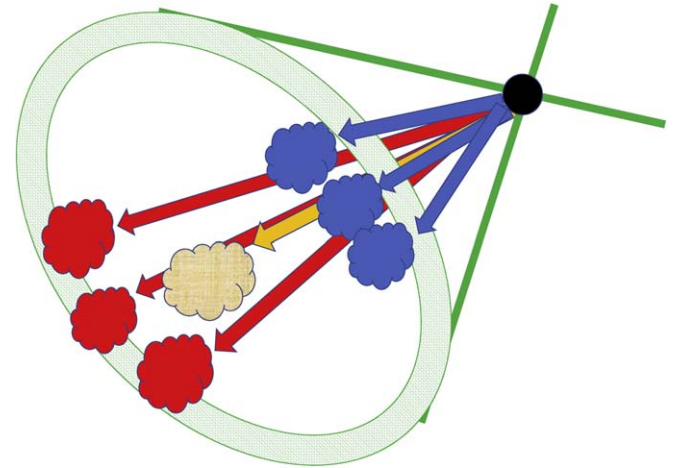
Figure 4. Plot of the median energy of a $1'' \times 0\rlap{.}''5$ box in (α, δ) for the 5.8–7.4 keV rest band. Blue "+" marks correspond to values from the observations of Mrk 34 with Chandra. A Chandra PSF simulation (red "X" marks) has no such linear energy-dependent trends, but rather an expected small increase with radius. The simulation has a median energy offset attributable to slightly different conditions in the PSF seed spectrum, which uses a smaller extraction radius ($r = 1''$ vs. $r = 2''$) and applies a point-source correction. The representative uncertainty (black cross) indicates the energy and spatial resolution ($\pm$ FWHM/2, with redshift correction for photon energy).

Figure 3. Top: multicolor image of the Mrk 34 nucleus binned at one-sixteenth native ACIS pixel scale, with $r = 0\rlap{.}''215$ Gaussian smoothing applied. White overlaid contours are from 8.44 GHz VLA imaging. Different image colors indicate the rest 5.8–6.3 keV band (red), 6.3–6.5 keV (green), and 6.5–7.4 keV (blue), as shaded in Figure 1. Centroid coordinates are indicated with black marks for the 3.2–5.8 keV rest band (box-circle), 5.8–6.3 keV (diamond), 6.3–6.5 keV (X), and 6.5–7.4 keV (+). Black circles show the centroid positional uncertainty. The diameter of the yellow solid circle indicates the FWHM of the Chandra PSF across these bands ($D \sim 0\rlap{.}''40$). White solid arrows indicate the direction and position angle of the fastest-moving optically emitting material according to Revalski et al. (2018). Bottom: as above, but data are adaptively smoothed to preserve features with at least nine photon counts.

Figure 5. Top: cartoon based upon Fischer et al.'s (2013) model, one of the possible models we consider (see also Figure 6). The observer is above the image and the SE cone is illustrated. Green indicates the bounds of the hollow biconical outflow seen in moderate-ionization optical ENLR gas (e.g., [O III]), which may be dominated by wind–ISM interactions. Arrows indicate the X-ray outflow velocity projected in the plane of the sky. Brown clouds have zero line-of-sight velocity relative to the host. Redshifted clouds (red) recede from the observer due to the geometry and inclination of the cone. Due to the inclination of the cone, their velocity projected to the observer is small relative to the wave band under consideration, allowing them to be detected. Blueshifted clouds (blue) approach the observer. Their velocity projected to the observer is large relative to the wave band and the clouds are undetected. In the NW cone the situation is similar but instead the blueshifted clouds remain in band. The X-ray outflows are interior to the conical bounds and retain a higher velocity than the optically emitting gas.

outflows for various reasons. First, the large EW of the red and blue wings ($\sim$[0.43, 0.99] keV) suggests reflection by the Kα transition of nearly neutral Fe species, such as might be found in dust, molecular clouds, or a moderately ionized X-ray wind (Kα transitions from $\lesssim$Fe XXI are confused with Fe I by the ACIS-S CCD).

A spatially resolved outflow could explain both red and blue wings via bilateral symmetry, similar to that seen from low-velocity outflows in optical and radio emission. If we assume the Fischer et al. (2013) biconical outflow model (SE, axial inclination $i = 25°$ toward the observer from the plane of the sky) and the blue–red N–S orientation of the Fe Kα wings, then the red and blue wings have the opposite projected velocities expected from a simple bulk outflow near the bicone axis. Figures 5 and 6 illustrate the velocity structure of this model in comparison with results from our data.
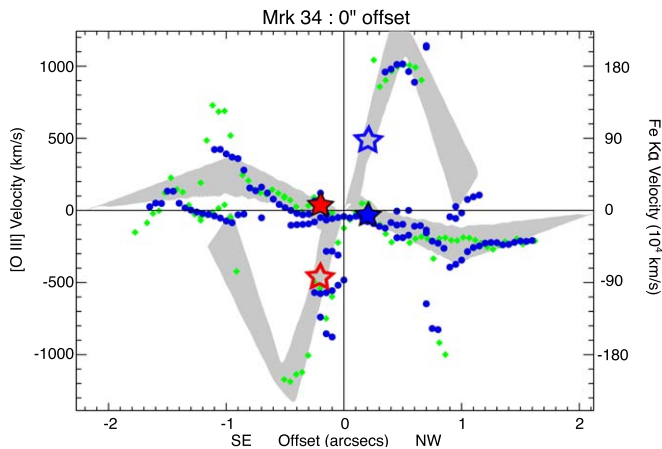
The velocity splitting produced by [O III] in the Fischer et al. (2013) outflow model suggests that the X-ray-emitting gas might also demonstrate velocity splitting due to a hollow conical structure. If so, the blue–red N–S orientation of the
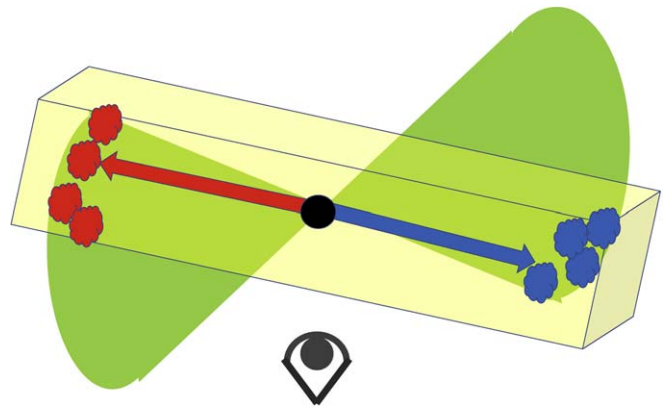
Figure 6. Figure 13 from Fischer et al. (2013), modified to illustrate the effects of an inclined hollow bicone geometry on projected velocities (see Figure 5). Green and blue circles represent [O III] velocities as observed by the Hubble Space Telescope, with velocity scale indicated on the left-side Y-axis. Gray shading represents the projected [O III] velocity structure of the bicone model. Red and blue filled stars indicate projected velocities measured by Chandra for the red and blue wings of Fe $K\alpha$, with velocity scale indicated on the right-side Y-axis. Red and blue empty stars indicate the unmeasured component corresponding to gas on the opposite exterior side of the hollow cone, with larger and opposite projected velocities.

Figure 7. Top: cartoon based upon Revalski et al. (2018, 2019), an alternative to the Fischer et al. (2013) model. The observer is at bottom looking up (dark gray). Green indicates the hollow biconical outflow seen in moderate-ionization optical ENLR gas (e.g., [O III]), which may be dominated by wind–ISM interactions. The yellow box is the plane of the galaxy, which is a large reservoir of gas for wind–ISM interactions. Red and blue indicate X-ray outflows seen in the red and blue wings of Fe $K\alpha$, which are redshifted and blueshifted accordingly. The X-ray outflows are interior to the conical bounds and retain a higher velocity than the optically emitting gas.

Fe $K\alpha$ wings requires them to be produced at an angle in the bicone that has a small inclination from the plane of the sky, i_{Fe}, and small projected velocities, such that $\theta_{min} - i \lesssim i_{Fe} \lesssim \theta_{max} - i$ (where $\theta_{min} = 30°$ is the inner opening angle and $\theta_{max} = 40°$ is the outer opening angle).

This model implies a negligible spatial deprojection, $\lesssim 4\%$ difference. The observed spatial extent of the Fe $K\alpha$ structure, $r \gtrsim 200$ pc, is $\gtrsim 100\times$ larger than the torus. The $r \lesssim 200$ pc region is associated with rapid radial increases in optical kinetic energy, kinetic power momentum, and momentum outflow, and the X-ray features we describe are interior to the associated turnovers in these quantities at $r \sim 500$ pc (Revalski et al. 2018, 2019).

Since $3.9 \lesssim (\sin i_{Fe})^{-1} \lesssim 11.5$, the median photon energy shift in Figure 4 (~ 150 eV) from the central bin corresponds to deprojected $0.09c \lesssim |v| \lesssim 0.26c$. The center of the best-fit Gaussian describing the red wing corresponds to $0.2c \lesssim |v| \lesssim 0.5c$ deprojected, and the velocity shift for the blue wing would have a similar value. For comparison, the fastest optically emitting material in Mrk 34 has a deprojected velocity of $v \sim 2000$ km s^{-1}, with the same [N, S] orientation for [blue, red] shifts.

Complementary counterpart features produced on the opposite side of the Mrk 34 cone are likely to be difficult to observe with Chandra given the corresponding projection angles. Redshifted Fe $K\alpha$ gas in the NW cone may suffer from obscuration by host ISM (e.g., a likely E–W nuclear dust feature seen by the Hubble Space Telescope, HST; Falcke et al. 1998), relativistic debeaming, and greater low-energy continuum from spatially confused emission. The energy response of Chandra ACIS drops more rapidly above ~ 7 keV than any gain from blueshifted Fe $K\alpha$ gas in the SE cone would fall, implying a $\lesssim 1\sigma$ detection for a red-wing counterpart projected at a blueshift of $v \gtrsim 0.2c$. By comparison, the $0.15 \lesssim E/6.39$ keV $- 1 \lesssim 0.50$ energy band (systemic; 7.0–9.1 keV observer) contains [4, 8] photons for $r \leqslant [0.''5, 1.''0]$, including continuum. This band's centroid is $\sim 0.''4$ south of the blue-wing centroid, and consistent with the southern feature in the red wing.

Unlike Fischer et al. (2013), Revalski et al. (2018, 2019) assume that the [O III] gas in Mrk 34 is confined to the plane of the galaxy (Figure 7). In this model, the velocity deprojection factor would only be ~ 1.56, implying deprojected $v \sim 0.08c$. This interpretation is complicated by the lack of measured [O III] outflow components with the appropriate blue/redshift direction at $r \lesssim 0.''5$, but, unlike Fischer et al. (2013), does not require explaining the nondetection of an opposite-shift counterpart in the same cone.

In either model, the deprojected velocities would be solidly in the regime of UFOs, which in X-rays have normally been seen (unlike Compton-thick Mrk 34) as absorption at $0.03c \lesssim v \lesssim 0.3c$ in an otherwise weakly obscured continuum, and commonly attributed to Fe XXV or Fe XXVI (Tombesi et al. 2010, 2014; Gofford et al. 2013; Chartas et al. 2021; but see also a P-Cygni–like profile in Nardini et al. 2015). The velocity structure of Mrk 34 suggests bulk motion $\gtrsim 12 - 30\times$ faster than the optical gas. With kinetic energy limits in the range KE$_{X-ray} \gtrsim 140 - 800 \times (M_{X-ray}/M_{optical})$, such gas could produce the kinetic power in the X-ray winds described by Trindade Falcão et al. (2021) with mass ratio limits in the range $M_{X-ray}/M_{optical} \lesssim 0.06 - 0.34$. Such winds might easily carry the bulk of the outflow kinetic energy and drive the acceleration of [O III] gas.

Since strong Fe $K\alpha$ is likely to require a large column density ($\log N_H \gtrsim 23$), it is likely to be associated with dusty molecular clouds. Such dense, low-ionization gas might then be converted into an [O III] wind expanding at larger radii, as per Trindade Falcão et al. (2021). As per the galaxy-scale outflows in IC 5063, such clouds may be launched from the ISM via ablation at small radii (Maksym et al. 2020, 2021; Travascio et al. 2021) and entrained, or near the plane of the galaxy. Alternately, high-velocity dust may originate in the AGN wind itself, as outflowing clouds condense to form molecular structures as they cool (Elvis et al. 2002).

4.2. Spatially Resolved Obscuration

Local column overdensities may contribute to some of the observed spatial structure. HST observations (Falcke et al. 1998) show evidence for dust lanes that cut E–W across the

nucleus. Such dust lanes could, for certain column densities, suppress the relatively soft continuum emission and red wing, e.g., at the spatial location of the blue wing. The blue wing is spatially coincident with the brightest radio hot spot, which may indicate the nucleus (such that deprojection may not be appropriate for the blue wing), but the absolute and relative astrometric uncertainty do not require this. If the blue wing is coincident with the nucleus, then the inferred radial extent is greater for the southern outflow (which is receding relative to the observer) but implies a larger radial extent for that outflow and implies a lack of a northern biconical counterpart.

4.3. Thermal Outflows

The blue-wing energy range is consistent with highly ionized Fe XXV at $v \lesssim 2000\,\mathrm{km\,s^{-1}}$, which corresponds to $v \lesssim 3000-22,000\,\mathrm{km\,s^{-1}}$ depending upon the deprojection model. Others have observed extended Fe XXV in association with strong AGN outflow–ISM shocks, e.g., NGC 6240 (Wang et al. 2014), NGC 4945 (Marinucci et al. 2017), and IC 5063 (Travascio et al. 2021). The proximity of the blue wing to the peak 8.44 GHz may point to a similar scenario in Mrk 34.

The spatial extent of the observed structure is consistent with that of optically emitting gas in a region where the kinetic power of the optically emitting gas rises steadily with increasing radius (Revalski et al. 2018, 2019). This could be true whether the blue wing were associated with the nucleus or offset from it. If the emission does originate from the continuum or highly ionized Fe XXV, then it may point to shocks in the hot component of a multiphase medium. Simulations by, for example, Mukherjee et al. (2018) indicate the presence of $kT \gtrsim 10^{8}$ K gas in IC 5063. Fe XXV in Mrk 34 suggests $kT \sim 10^{7.5}$ K, and for Fe XXVI to be negligible kT would be narrowly constrained.

One major difficulty in this scenario includes the large wing EW. In addition, the red-wing emission is particularly difficult to explain via Fe XXV, requiring deprojected $v \gtrsim 0.4c$. If associated with bipolar outflows, such a feature may leave similarly blueshifted features at other energies (possibly via other species), which we have not been able to identify.

In principle, "back-streaming" from jet–ISM interactions could cause a combination of low-velocity and high-velocity features. For example, Das et al. (2005) claim such effects for faint, high-velocity [O III] clouds in NGC 4151 as the result of shocks. If some of the red and blueshifted Fe line emission is colocated (such as with the northern component of the spatially bifurcated red wing, which is spatially consistent with the blue wing and the brightest radio hot spot) then Fe XXV and possibly Fe XXVI could be formed at a shock, while redshifted emission could be part of the backflow.

4.4. An Obscured Relativistic Jet

Bremsstrahlung from a relativistic jet at the nucleus might mimic an excess spanning the red and blue wings when obscured by Compton-thick material. Such an excess might be variable on observable timescales, and would appear as continuum emission at microcalorimeter (e.g., XRISM or Athena) resolution. Doppler effects from sufficiently relativistic extended outflows (either a wind or jet) might affect assumptions of spatial symmetry.

5. Conclusion

The spatially and spectrally extended X-ray emission associated with the Fe Kα complex of Mrk 34 is likely associated with the well-known powerful, kiloparsec-scale outflows that have been studied in optical and radio emission. This X-ray emission is likely due to redshifted and blueshifted Fe Kα fluorescence and may be associated with molecular clouds at the brightest radio knots, near the base of the outflow. Some of this emission may be associated with shock emission from a hot collisionally ionized plasma that also produces highly ionized Fe XXV, as has been observed in IC 5063 (Travascio et al. 2021).

In any event, the source of the emission is likely to be expanding from the nucleus at a velocity a factor of $\gtrsim 12$–28 greater than outflows observed in optical spectroscopy. Regardless of the specific origin of the part of emission, then, it is likely to be a multiphase medium with fast-moving hot gas, which may indicate a critical link between subparsec-scale UFOs previously seen in absorption, as well as ∼kiloparsec-scale feedback mechanisms. Using Chandra observations of NGC 5728, Trindade Falcão et al. (2023a, 2023b) have recently demonstrated a new example of emission attributable to Fe Kα emission which is spatially and spectrally extended, and suggestive of UFOs on $\lesssim 200$ pc scales. Although several aspects of the specific physical interpretation remain uncertain, their work demonstrates larger spatial extent, superior photon statistics, and confirms the existence of systems with properties similar to those we attribute to this novel Fe Kα complex in Mrk 34. Such interactions between the hot outflows and dense molecular clouds near the nucleus may form the base of the expanding [O III] and X-ray winds via similar mechanisms to those described by Trindade Falcão et al. (2021).

New observations are necessary to better describe the origins of this extended emission. Deeper imaging spectroscopy with Chandra or a high-resolution implementation of AXIS would provide better statistical constraints on these models, and microcalorimeter spectroscopy from XRISM or Athena would spectrally resolve composite nuclear models. NuSTAR may constrain the presence of a line-of-sight component for the biconical outflow. Lynx is necessary to unambiguously associate reliable emission models with the spatial features described here. Imaging spectroscopy with JWST and the Next Generation VLA is necessary to investigate the roles of outflowing molecular gas and moderately ionized winds, both of which are likely present, regardless of the specific Fe excitation mechanisms.

ORCID iDs

W. Peter Maksym ⓘ https://orcid.org/0000-0002-2203-7889
Martin Elvis ⓘ https://orcid.org/0000-0001-5060-1398

Giuseppina Fabbiano ⓘ https://orcid.org/0000-0002-3554-3318
Anna Trindade Falcão ⓘ https://orcid.org/0000-0001-8112-3464
Steven B. Kraemer ⓘ https://orcid.org/0000-0003-4073-8977
Travis C. Fischer ⓘ https://orcid.org/0000-0002-3365-8875
D. Michael Crenshaw ⓘ https://orcid.org/0000-0002-6465-3639
Thaisa Storchi-Bergmann ⓘ https://orcid.org/0000-0003-1772-0023

References

Ahn, C. P., Alexandroff, R., Allende Prieto, C., et al. 2012, ApJS, 203, 21
Arav, N., Liu, G., Xu, X., et al. 2018, ApJ, 857, 60
Arnaud, K. A. 1996, XSPEC: The First Ten Years, in ASP Conf. Ser. 101, ed. G. H. Jacoby & J. Barnes, 17
Baloković, M., Brightman, M., Harrison, F. A., et al. 2018, ApJ, 854, 42
Bessiere, P. S., & Ramos Almeida, C. 2022, MNRAS, 512, L54
Cash, W. 1979, ApJ, 228, 939
Chartas, G., Cappi, M., Vignali, C., et al. 2021, ApJ, 920, 24
Das, V., Crenshaw, D. M., Hutchings, J. B., et al. 2005, AJ, 130, 945
Davis, J. E., Bautz, M. W., Dewey, D., et al. 2012, Proc. SPIE, 8443, 84431A
Elvis, M., Marengo, M., & Karovska, M. 2002, ApJL, 567, L107
Fabbiano, G., Elvis, M., Paggi, A., et al. 2017, ApJL, 842, L4
Fabbiano, G., Paggi, A., Karovska, M., et al. 2018a, ApJ, 855, 131
Fabbiano, G., Paggi, A., Karovska, M., et al. 2018b, ApJ, 865, 83
Fabbiano, G., Siemiginowska, A., Paggi, A., et al. 2019, ApJ, 870, 69
Falcke, H., Wilson, A. S., & Simpson, C. 1998, ApJ, 502, 199
Fischer, T. C., Crenshaw, D. M., Kraemer, S. B., et al. 2013, ApJS, 209, 1
Fischer, T. C., Machuca, C., Diniz, M. R., et al. 2017, ApJ, 834, 30
Fornasini, F. M., Elvis, M., Maksym, W. P., et al. 2022, ApJ, 931, 65
Fruscione, A., McDowell, J. C., Allen, G. E., et al. 2006, Proc. SPIE, 6270, 62701V
Gandhi, P., Lansbury, G. B., Alexander, D. M., et al. 2014, ApJ, 792, 117
Gaspari, M., & Sądowski, A. 2017, ApJ, 837, 149
Gofford, J., Reeves, J. N., Tombesi, F., et al. 2013, MNRAS, 430, 60
Harrison, C. M., Costa, T., Tadhunter, C. N., et al. 2018, NatAs, 2, 198
Hopkins, P. F., & Elvis, M. 2010, MNRAS, 401, 7
Jones, M. L., Fabbiano, G., Elvis, M., et al. 2020, ApJ, 891, 133
Jones, M. L., Parker, K., Fabbiano, G., et al. 2021, ApJ, 910, 19
Joye, W. A., & Mandel, E. 2003, New Features of SAOImage DS9, in ASP Conf. Ser. 295, ed. H. E. Payne, R. I. Jedrzejewski, & R. N. Hook, 489
Laha, S., Reynolds, C. S., Reeves, J., et al. 2021, NatAs, 5, 13
Loredo, T. J. 1992, in SCMA (State College, PA: PSU), 275
Ma, J., Elvis, M., Fabbiano, G., et al. 2020, ApJ, 900, 164
Maksym, W. P., Fabbiano, G., Elvis, M., et al. 2017, ApJ, 844, 69
Maksym, W. P., Fabbiano, G., Elvis, M., et al. 2019, ApJ, 872, 94
Maksym, W. P., Fabbiano, G., Elvis, M., et al. 2021, ApJ, 917, 85
Maksym, W. P., Schmidt, J., Keel, W. C., et al. 2020, ApJL, 902, L18
Marinucci, A., Bianchi, S., Fabbiano, G., et al. 2017, MNRAS, 470, 4039
Mukherjee, D., Wagner, A. Y., Bicknell, G. V., et al. 2018, MNRAS, 476, 80
Nardini, E., Reeves, J. N., Gofford, J., et al. 2015, Sci, 347, 860
Nenkova, M., Sirocky, M. M., Ivezić, Ž., et al. 2008, ApJ, 685, 147
Nenkova, M., Sirocky, M. M., Nikutta, R., et al. 2008, ApJ, 685, 160
Revalski, M., Dashtamirova, D., Crenshaw, D. M., et al. 2018, ApJ, 867, 88
Revalski, M., Dashtamirova, D., Crenshaw, D. M., et al. 2019, ApJ, 881, 167
Serafinelli, R., Tombesi, F., Vagnetti, F., et al. 2019, A&A, 627, A121
Tombesi, F., Cappi, M., Reeves, J. N., et al. 2010, A&A, 521, A57
Tombesi, F., Tazaki, F., Mushotzky, R. F., et al. 2014, MNRAS, 443, 2154
Travascio, A., Fabbiano, G., Paggi, A., et al. 2021, ApJ, 921, 129
Trindade Falcão, A., Fabbiano, G., Elvis, M., et al. 2023a, ApJ, 950, 143
Trindade Falcão, A., Fabbiano, G., Elvis, M., et al. 2023b, arXiv:2303.00782
Trindade Falcão, A., Kraemer, S. B., Fischer, T. C., et al. 2021, MNRAS, 505, 3054
Wang, J., Nardini, E., Fabbiano, G., et al. 2014, ApJ, 781, 55
Zhao, X., Marchesi, S., Ajello, M., et al. 2020, ApJ, 894, 71